Chapter 4 Results and Discussion

The results on (001) epitaxial IrMn/CoFe system are presented in this chapter. There are two parts in the chapter: (1) deposition methods and film structural characterization, and (2) magnetic properties including the magnetization reversal behaviors and the unusual time-dependent effect of (001) IrMn/CoFe system.

4.1 The growth of (001) Epitaxial IrMn/CoFe on Si(001)

4.1.a Introduction

In our experiment, the composition of IrMn alloy is $Ir_{20}Mn_{80}$, corresponding to the γ-phase disordered and face-centered cubic (fcc) structure with lattice constant a_1=3.78 Å. On the other hand, the alloy of $Co_{50}Fe_{50}$ has the body-centered cubic (bcc) structure with the lattice constant a_2=2.87 Å. The lattice mismatch between a_1 and $\sqrt{2}\,a_2$ is 7.4%, which means CoFe may have chance to grow epitaxially on IrMn film by rotating 45°, as illustrated in Fig. 4.1(a). Therefore, in order to obtain high (001) preferred orientation of IrMn/CoFe films, it is necessarily to find out an appropriate (small lattice mismatch) substrate or buffer layers whose crystal structures are the same as those of CoFe and IrMn.

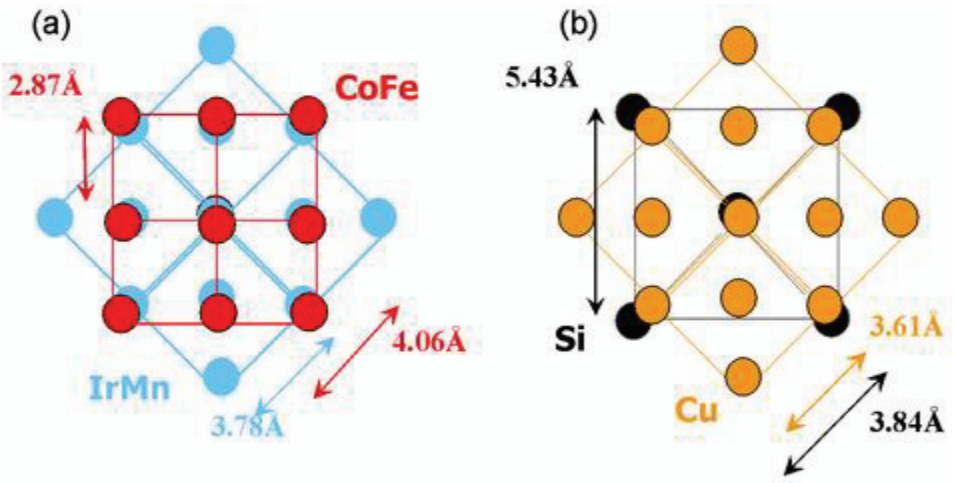

Fig. 4.1 (a) The possible epitaxial relationship between IrMn and CoFe, the lattice mismatch between a_{IrMn} and $\sqrt{2}\, a_{CoFe}$ is 7.4%. (b) The epitaxial relationship between Cu and Si (001) was found to be Si (001)//Cu (001) and Si [110]//Cu [010].

4.1.b Experiment Procedure

Based on Metal-Metal Epitaxy on Silicon (MMES) technique, we used (001) Cu as underlayers to deposited (001) $Ir_{20}Mn_{80}$ and $Co_{50}Fe_{50}$ layers because of the lattice mismatch of Cu/IrMn and IrMn/CoFe were 4.6% and 7.4%, respectively. Before depositions, Si wafers were first cleaned by using acetone to degrease and put into 10 % HF solution for several seconds, followed by rinsing in deionized water and drying by N_2 ,and then the wafers were loaded into the sputtering chamber immediately. The HF treatment was the key step for the epitaxial growth of Cu on Si (001). After dilute HF dipping, Si surface was found to be hydrogen terminated with a (1×1) reconstruction [1,2], which is the essential condition for Cu epitaxy on Si, as described in the previous section. During the deposition, all films were processed at ambient temperature with the rate of about 1 Å/s. The working pressure is 3mTorr while the base pressure is 6.0×10^{-7} Torr.

In 1990, Chang reported that by using electron beam evaporation without intentional heating of the substrates, (001) and (111) Cu epitaxial films can be grown on hydrogen terminated (001) and (111) Si, respectively [3]. Furthermore, it is of interest to use the Cu film as the seed layer for additional epitaxial growth of metal films. The growth of metal films with the (001) orientation for both fcc and bcc metals, starting with the (001) Cu films epitaxially grown on (001) Si as seed layers, was reported. The fcc metals grown by this technique include Ni, Co [4], Rh, Ir, Pd, Au, Ag, Pt [5], and Al [6], and the bcc metals include Fe, Cr, V, Mo, W [7]. This technique was called metal-metal epitaxy on silicon (MMES). Indeed, the epitaxial growth of Cu on Si was found to depend on the cleanliness of the silicon substrate surface, as in (001) epitaxial films, (001) Cu can only grow on hydrogen terminated Si (001) reconstructed surface [8]. Furthermore, it has been shown that such hydrogen terminated surfaces are known to be inert for several minutes in air and for several hours in high vacuum at room temperature [9]. This surface passivation is believed to be due to hydrogen termination of the dangling Si bounds, which renders the chemically stable surface [10]. During the growth of Cu on Si (001) at room temperature, it was found that interdiffusion between Cu and Si occurred within a region about 100 Å, resulting in the formation of Cu_3Si silicide, which adjusted the lattice mismatch between Cu and Si [11]. The epitaxial relationship between Cu and Si (001) was found to be Si (001)//Cu (001) and Si [110]//Cu [010], as schematically illustrated in Fig. 4.1(b). Since the crystal structure of Cu is fcc with the lattice constant of a=3.615Å, we can use this technique to grow (001) epitaxial IrMn/CoFe films.

4.2 Structural Characterization

The films of Si(001)/Cu/IrMn/CoFe/Ta were firstly characterized by X-ray diffraction with the wavelength of Cu K_α. Furthermore, to verify the in-plane orientation and the epitaxial relationships between layers, asymmetric in-plane φ scans were performed in a four-circle X-ray diffractometer, which has been introduced in the preceding chapter.

Structural Characterization of (001) IrMn/CoFe system

Fig. 4.2 shows the X-ray θ-2θ results of Si(001)/ Cu(Xnm)/ $Ir_{20}Mn_{80}$(10nm)/CoFe(4nm)/Ta(4nm) deposited by dc magnetron sputtering. The Cu thickness was varied from 20 to 80 nm. We can clearly see that with increasing the thickness of Cu, the stronger (200) peaks of both Cu (2θ=50.74°) and IrMn (2θ=47.74°) were observed. In addition, a very small signal was observed at around 65°, seen in the inset of the figure, corresponded to the CoFe (200). Therefore, to distinctly observe the (200) CoFe peak, the samples with Si(001)/ Cu(80nm)/ IrMn(20nm)/ CoFe(Xnm)/ Ta(4nm) was investigate by varying the CoFe thickness from 12 to 20nm. As show in the Fig. 4.3, the stronger peak of CoFe (2θ=65.04°) was obtained by increasing the CoFe thickness, indicating that the sample are of a good out of plane (001) texture. Then we calculated the lattice constants according to the peak positions of Cu, IrMn, and CoFe are 3.6 Å, 3.81 Å, and 2.86 Å, respectively.

To verify the in-plane orientation and the epitaxial relationships between layers, asymmetric in-plane φ scans were performed in a four-circle X-ray diffractometer. The result is shown in Fig. 4.4, only four {111} diffraction peaks were detected, revealing the four fold symmetry of a cubic (001) epitaxial film. In addition, the {111} diffraction peaks of Cu and IrMn appear at the same φ angles, indicating a "cubic on cubic" orientation relationship since the structures of these films are both fcc structure and their lattice constants are similar. However, from the {111} peaks of CoFe and Si shown in Fig. 4.4(a) and (d), respectively, the peaks of CoFe and Si shift 45° from those of IrMn and Cu, which means that the epitaxial relationships are: Si(001)// Cu(001)// IrMn(001)// CoFe(001) and Si[110]// Cu[100]// IrMn[100]// CoFe[110].

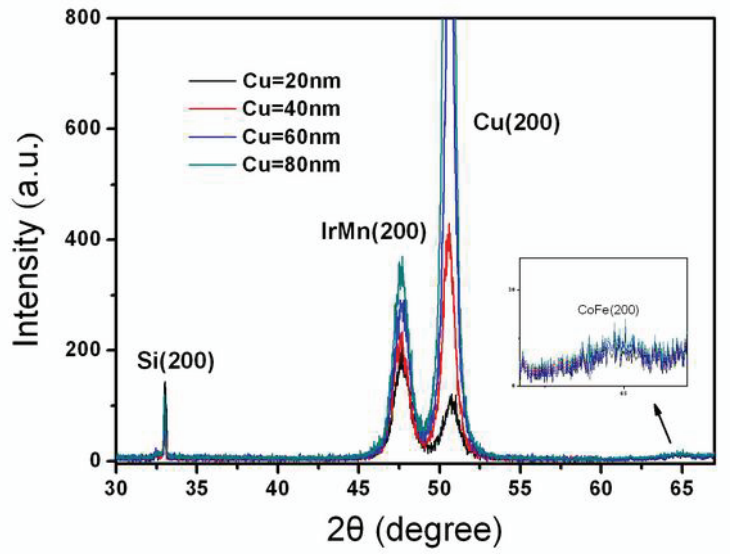

Fig. 4.2 The X-ray θ-2θ results of Si(001)/ Cu(Xnm)/ $Ir_{20}Mn_{80}$(10nm)/ CoFe(4nm)/ Ta(4nm). The stronger (200) peaks of both Cu (2θ=50.74°) and IrMn (2θ=47.74°) were observed with increasing the Cu thickness. In addition, the inset shows a very small signal of (200) CoFe at around 65°.

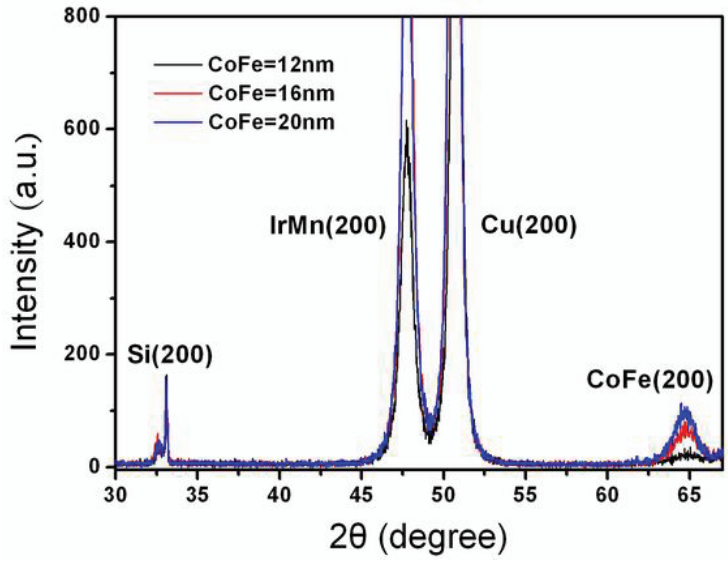

Fig. 4.3 The samples with Si(001)/ Cu(80nm)/ IrMn(20nm)/ CoFe(Xnm)/ Ta(4nm) the stronger peak of CoFe (2θ=65.04°) was obtained with increasing the CoFe thickness. The calculated the lattice constants according to the peak positions of Cu, IrMn, and CoFe are 3.6 Å, 3.81 Å, and 2.86 Å, respectively.

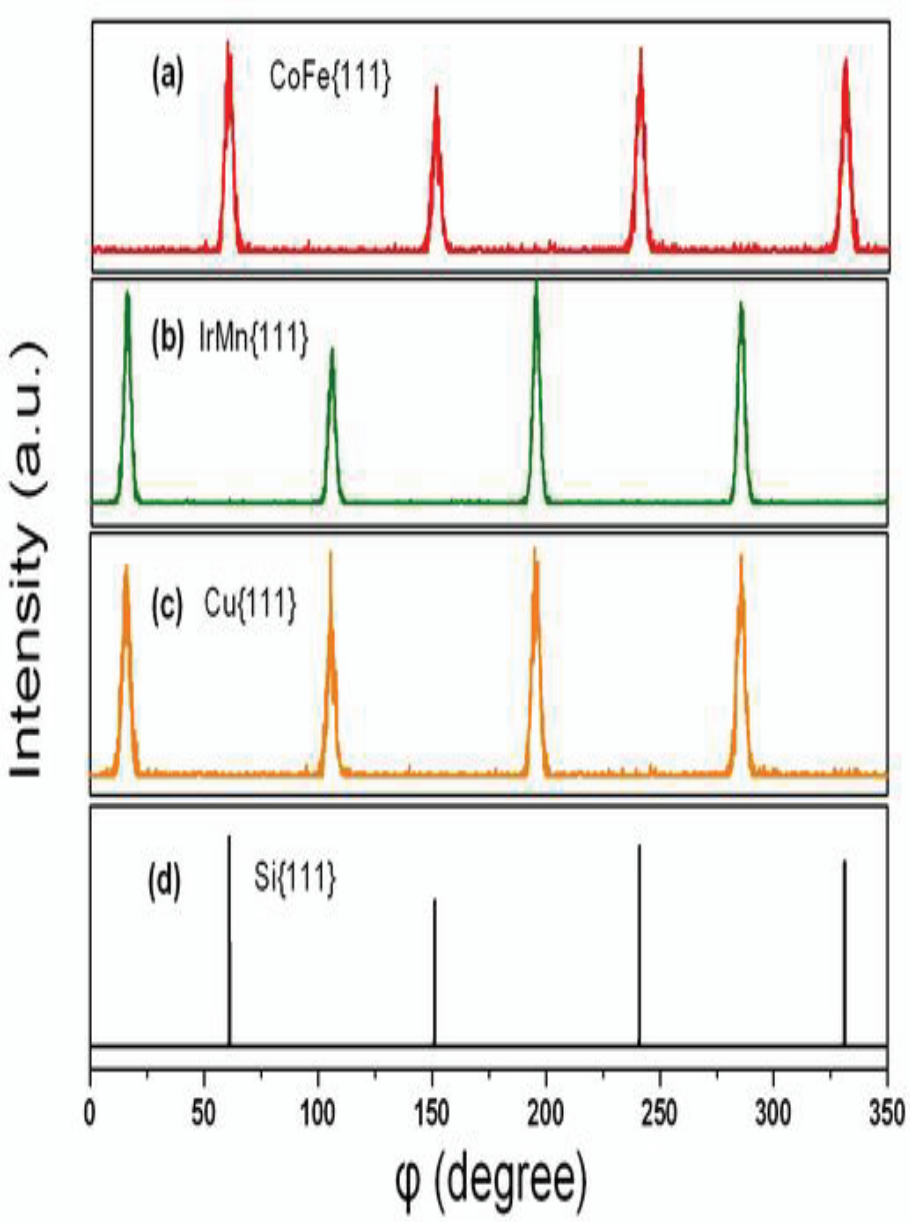

Fig. 4.4 X-ray φ scans of (a) CoFe {111}, (b) IrMn {111}, (c) Cu {111}, and (d) Si {111}. In addition, the shifted peaks indicate that the epitaxial relationships are: Si(001)// Cu(001)// IrMn(001)// CoFe(001) and Si[110]// Cu[100]// IrMn[100]// CoFe[110].

4.3 Magnetic Properties

4.3.a Annealing Effect

At the beginning of our investigation to the exchange anisotropy in (001) IrMn/CoFe system, the ex-situ post field annealing along CoFe [110], which was defined as the easy axis (θ=0°) of ferromagnetic layers, was performed in order to obtain a unidirectional anisotropy. Two annealing temperature of 200°C and 280°C were carried out for 20 minutes under an applied field of 1000 Oe, then cooled to the room temperature. Fig. 4.5 represents the X-ray results of structure change after annealing, compared to the as-deposited films, no Cu (002) diffraction peak was observed because Cu-Si silicide (Cu_3Si) was formed during the high annealing temperature. Besides, due to the diffusion of Cu and Si atoms [12], the IrMn (200) peaks also decrease significantly with increasing the annealing temperature.

Since the structure destruction by post field annealing, an external field of 170 Oe along CoFe [110] was applied to achieve unidirectional anisotropy without the post-annealing procedure.

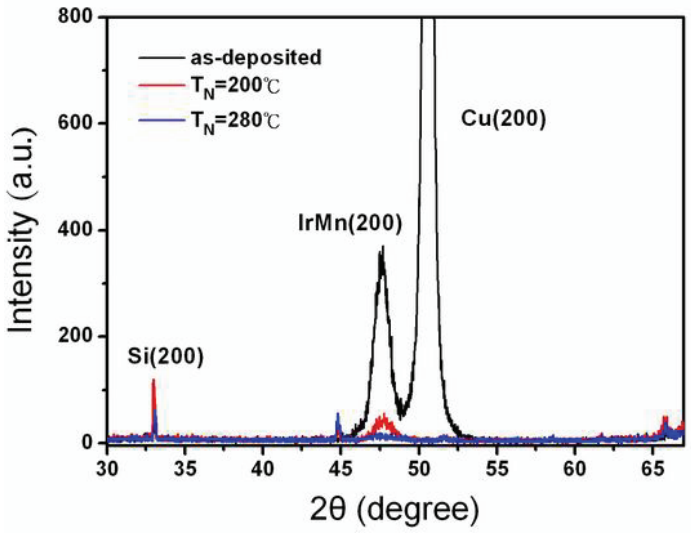

Fig. 4.5 The X-ray results of structure change after annealing, no Cu (002) diffraction peak was observed because Cu-Si silicide (Cu_3Si) was formed during the high annealing temperature

4.3.b Exchange anisotropy in (001) epitaxial IrMn/CoFe system

In this section, we have investigated the exchange anisotropy in (001) IrMn/CoFe system by varying the thickness of IrMn. Samples of Si(001)/ Cu(50nm)/ $Ir_{20}Mn_{80}$(Xnm)/ $Co_{50}Fe_{50}$(15nm)/ Ta(6nm) were deposited by dc magnetron sputtering. The IrMn thickness was varied from 5 to 40 nm. The details of sample preparation were discussed in the previous section. During the deposition, some samples were deposited at a presence of an external field of 170 Oe parallel to the film plane along CoFe [110], which was defined as the easy axis (θ=0°) of ferromagnetic layers. All of the depositions were processed at ambient temperature and no post-annealing was performed. The magnetic properties of the samples were measured by

vibrating sample magnetometer (VSM), equipped with two sets of orthogonal pick-up coils, which made it possible to simultaneously measure both of the longitudinal and transverse magnetization curves.

Results

The hysteresis loops of IrMn(20nm)/CoFe(15nm) deposited without a field, showed a four-fold symmetry, which indicated a perfect bi-axial anisotropy with the easy axis along CoFe <110> and the hard axis along <100>, as depicted in Fig. 4.6. The biaxial crystalline anisotropy constant can be determined by the formula $K_b=(H_{sat}\times M_s)/2$, where H_{sat} is the saturation field along the hard axis and M_s is the saturation magnetization of CoFe. From Fig. 4.6, we can approximately estimate the K_b value of 4.56×10^5 erg/cm^3 by setting the H_{sat}=570 Oe and M_s=1600 emu/cm^3 . The value is close to the reported data [13].

On the other hand, for the samples deposited in an external field, a square loop with an exchange bias field (H_E) was observed along CoFe [110], but the loops measured along CoFe[1-10] exhibit unusual double shifted magnetization curve (Fig. 4.7). As increasing the IrMn thickness, both the exchange bias field (H_E) and the separation of the double shifted loop ($2H_S$) increase. Meanwhile, the coercivity of CoFe decreases with the increasing of the IrMn thickness. Fig. 4.8(a) shows the exchange bias field (H_E), coercivity (H_C), and the shift field (H_S) of (001) IrMn/CoFe for different IrMn thickness.

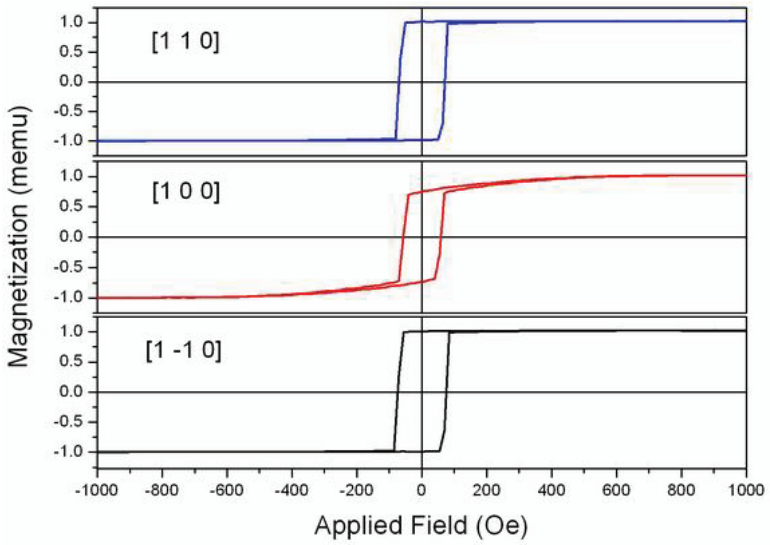

Fig. 4.6 The hysteresis loops of IrMn(20nm)/CoFe(15nm) deposited without a field, indicated a perfect bi-axial anisotropy with the easy axis along CoFe <110> and the hard axis along <100>.

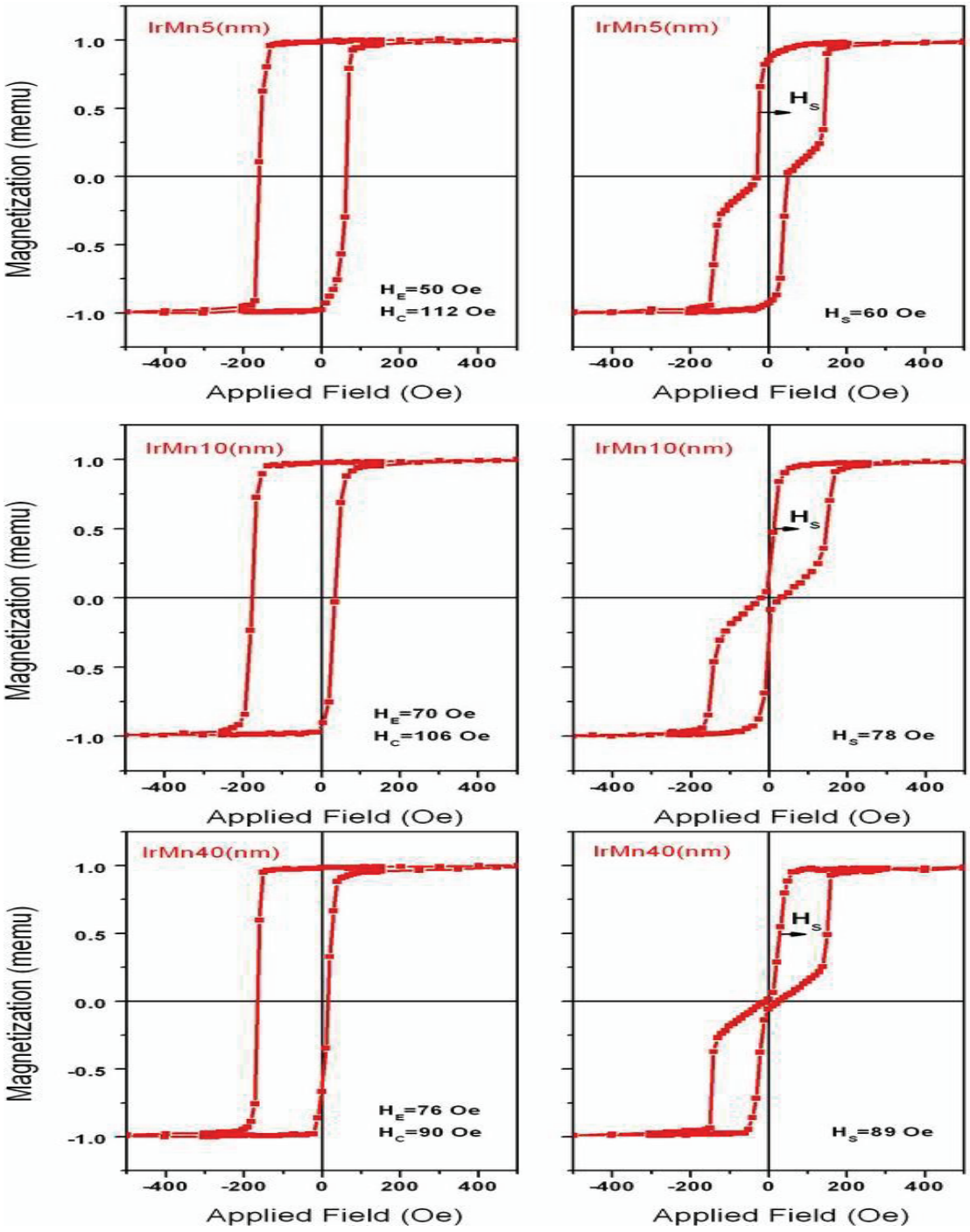

Fig. 4.7 Hysteresis loops of different IrMn thickness, the square exchange bias loops of left hand side were measured along the easy axes of CoFe; i.e. [110]. On the other hand, the double shifted loops of right hand side were observed by measured along CoFe [1-10].

Discussion

Actually, the formation of the double shifted loops can be understood with the Stoner-Wohlfarth theory of the appropriate ratio of the $K_b + K_u$ to K_b [14,15], where K_b and K_u are the magnetocrystalline (biaxial) crystalline and uniaxial anisotropy constants, respectively. In the previous report, the double shifted magnetization curves were observed with the random steps at interface or miscut substrates because of the fourfold symmetry locally broken by a step-induced uniaxial symmetry, K_u [16]. In our case, since the IrMn/CoFe system only revealed the biaxial anisotropy for the films deposited without external field, the double shifted magnetization curves of (001) IrMn/CoFe system can be understood as the break of four fold symmetry by applied an external field during the deposition.

Considering the Stoner-Wohlfarth (coherent rotation) model, the energy of CoFe per unit volume, E(erg/cm^3), can be express as：

$$\mathbf{E = -M_S \bullet H-(K_e/t_F)\cos\theta+K_u\sin^2\theta+K_b\sin^2\theta\cos^2\theta} \qquad (1)$$

where **H** is the applied field; $\mathbf{t_F}$ is the thickness of CoFe; $\mathbf{K_e}$(erg/cm^2) is the unidirectional anisotropy constant, equal to $H_eM_St_F$ ($\mathbf{H_e}$ is the exchange field); $\mathbf{K_u}$ is the uniaxial anisotropy constant; $\mathbf{K_b}$ is the biaxial crystalline anisotropy constant. $\boldsymbol{\theta}$ is the angle between magnetization and CoFe[110]. The anisotropies were calculated by the numerical calculation based on Stoner-Wohlfarth model. $\mathbf{K_u}$ and $\mathbf{K_b}$ were obtained by the best fitting of hysteresis loops at $\boldsymbol{\theta}$**=90**°[14,17], in which the magnetization reversal is purely rotational.

For samples with a small thickness of IrMn, when the magnetization of CoFe rotated, it may drag the unpinned interfacial IrMn spins irreversibly, which contributed to enhanced coercivity (Hc) and uniaxial anisotropy K_u of CoFe (Fig. 4.8(b)). With increasing the thickness of IrMn, the total anisotropy energy of IrMn ($K_{IrMn}V_{IrMn}$) increased so the spins of IrMn were more stable and not easily rotated when the magnetization of CoFe was reversed. Consequently, the increased exchange field and K_e was observed; meanwhile, increased unidirectional anisotropy broke the pure biaxial symmetry so H_s increased with H_e .On the other hand, the biaxial crystalline anisotropies were almost the same, consistent with the fact that the K_b was independent of the thickness of IrMn.

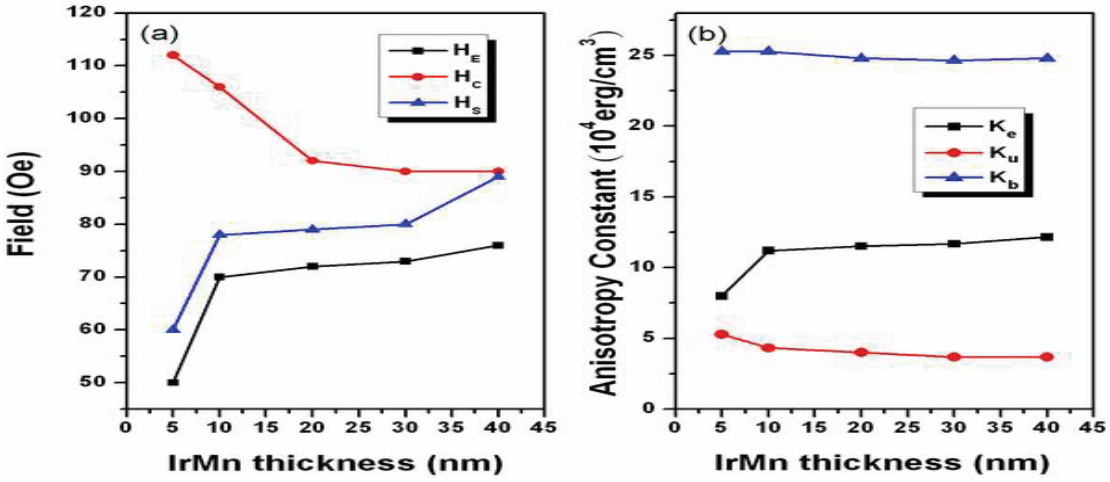

Fig. 4.8 (a) Variation of coercivity (H_c), exchange field(H_e) and half of separation of the double-shifted loop (H_s) with different thickness of IrMn (b)IrMn thickness dependence of unidirectional (K_e), uniaxial (K_u) and biaxial (K_b) anisotropy constants.

The hysteresis loops measured from a vector coil, a pick-up coil locating in the orthogonal direction (y-direction) to the applied field direction (x-direction), provide understanding of magnetization reversal in the (001) IrMn/CoFe system. Considering the sample of IrMn(5nm)/CoFe(15nm), there was almost no signal observed in the y direction ([1-10]) when the field was applied along easy axis ([110]), shown in Fig. 4.9(a). This result indicates that the magnetization of CoFe reverses by nucleation and growth of reversed domains with the magnetization along the easy axis. On the other hand, unlike conventional exchange-biased bilayers, a local energy minimum exists at [1-10] and [-110] of (001) IrMn/CoFe system due to the four-fold crystalline anisotropy; therefore, the M_y loop exhibits a two-stage reversal in the hard axis. When a negative saturation field was applied along the hard axis (-90°), CoFe magnetization first stayed around its local minimum. With a critical field, magnetization abruptly rotated to the universal energy minimum of [110] (0°) due to unidirectional anisotropy (shown in M_x curve); therefore, a strong M_y signal was observed. With further increasing a positive field, a gradual magnetization rotation occurred, and finally magnetization suddenly switched to 90^o (Fig. 4.9(b)).

To further characterize the magnetization reversal along the hard axis, shown in Fig. 4.9(b), we plotted the angular dependence of energy curves by using Eq. (1). Each curve in Fig. 4.10 corresponds to one applied field. Since the magnetization stays at its energy minimum state, the critical angles and applied fields for the magnetization switching can be obtained explicitly. With decreasing the applied field from the negative saturation field (state1 to state3), the magnetization of CoFe reversibly rotates from its initial stable

state ([1-1 0] (-90°), state 1). When the field reaches 12 Oe (state 4), the magnetization is in a metastable state, that is, the magnetization rotates to [110] (0°, state 5) with a slightly increasing field. The state 4 corresponds to a critical angle of -70°. Subsequently, the magnetization reversibly rotates around [110] (state 6) until the field reaches 145 Oe (state 7), at which the magnetization irreversibly rotates again to the angle near [-1 1 0] (state8). The critical angle corresponding to state 7 is 30°. The anisotropy constants in these calculations are $K_e/t_F=8.0\times10^4 erg/cm^3$, $K_u=5.28\times10^4 erg/cm^3$, and $K_b=2.53\times10^5 erg/cm^3$, which are obtained from the best-fitted M_x curve, shown in the Fig. 4.9 (b). These calculations also reveal that under the competition of K_e, K_u and K_b, the two-stage magnetization reversal exists and the range of state5 to state7 mainly depends on the magnitude of unidirectional anisotropy (K_e).

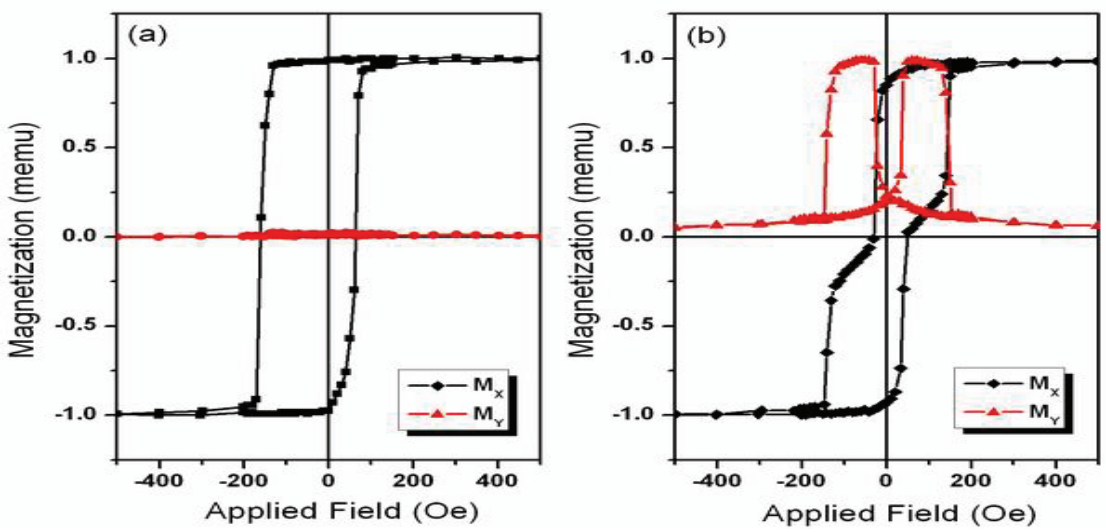

Fig. 4.9 Hysteresis loops of Si(100)/Cu(50nm)/$Ir_{20}Mn_{80}$(5nm)/CoFe(15nm)/ Ta(4nm) deposited in a field, measured along CoFe (a) [110] and (b) [1-10]. The M_x and M_y curves were measured along the applying field direction and along the direction orthogonal to the applying field, respectively.

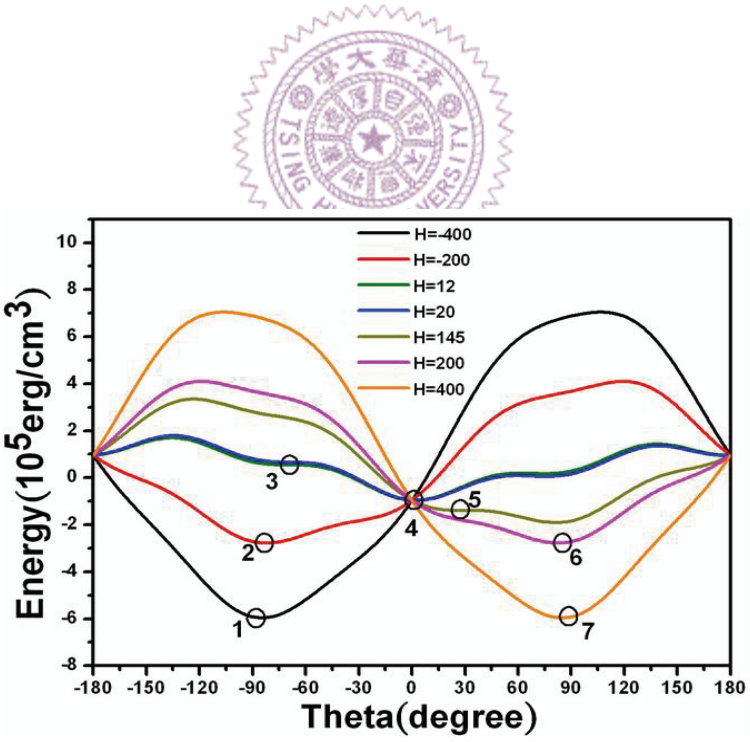

Fig. 4.10 The energy curves calculated by using coherent rotational model. The sample structure is IrMn(5nm)/ CoFe(15nm).

4.3.c Angular Dependence of Magnetization Reversal in (001) IrMn/CoFe

In exchange coupled ferromagnetic (FM)/antiferromagnetic (AF) systems, a common observation of the asymmetric hysteresis loops due to asymmetric magnetization reversal processes has been mentioned in chapter 2. Even though this asymmetry is now observed in magnetometry measurements of a number of material systems, much progress in understanding the associated reversal mechanisms has been based on recent studies of a model thin film system TMF_2/Fe (TM is transition metal) [18,19]. However, integral to this interpretation of EB in TMF_2/Fe systems is also the presence of a twinned microstructure of the TMF_2 antiferromagnet. Recently, the phenomenon of asymmetric magnetization reversal is more general by using high quality of epitaxial samples of an alternative model system, (001) MnPd/Fe, where the underlying antiferromagnet is a single crystal and not twinned in microstructure [20]. In this report, the direct images of the remnant magnetic domain structure probing by X-ray photoemission electron microscopy (PEEM) were performed. For the (001) MnPd/Fe, a strong biaxial crystalline anisotropy of ferromagnetic layer with the easy axes along Fe <100> is parallel to the directional of unidirectional anisotropy (Fe[100]). When the applied field is parallel to Fe [110]; i.e. 45° with respect to the bias direction (Fe[100]), the asymmetric magnetization reversal occurs by moment rotation for decreasing fields while it proceeds by domain nucleation and growth for increasing fields.

In our experiment, the hysteresis loops were measured in different angles between $\boldsymbol{\theta}$=0° and 90° while the loops in the same angles were fitted by using the Stoner-Wohlfarth (coherent rotation) model. In comparison with

the experimental hysteresis loops to the simulation ones, we have also observed the similar behaviors of asymmetric magnetization reversal.

Discussion

1. Symmetric Magnetization Reversal

Basically, it is now understood that the asymmetric magnetization reversal occurs by domain-wall motion on one side of the hysteresis loop and by magnetization rotation on the opposite side. In the contrast, magnetization reversal is symmetric when the process takes place by coherent rotation or domain wall motion) for both the increasing and decreasing field sweeping direction of the hysteresis loop. As the discussion in the preceding section, it has been suggested that the magnetization of CoFe reverses by nucleation and growth of reversed domains with the magnetization along the easy axis of CoFe [110] ($\boldsymbol{\theta}$=0°), while the magnetization reversal behaves as coherent rotational in the CoFe [1-10] ($\boldsymbol{\theta}$=90°). Fig. 4.11 shows the hysteresis loops of $\boldsymbol{\theta}$=0° and 90°, compared with the simulation curves, the best fitted curve by using the Stoner-Wohlfarth (coherent rotation) model is obtained at $\boldsymbol{\theta}$=90° due to its purely rotational behavior. However, considering to the loops at $\boldsymbol{\theta}$=0°, the coercivity (H_C) difference for increasing field branch ($H_{C1\ right}$- $H_{C2\ right}$) is equal to that of the decreasing one ($H_{C1\ left}$- $H_{C2\ left}$), also indicating a symmetric magnetization reversal by domain wall motion for both field branches of the loop. Therefore, we can conclude that the magnetization reversal at $\boldsymbol{\theta}$=0° and 90° are symmetric since their magnetization proceeds by purely domain wall motion and coherent rotation, respectively.

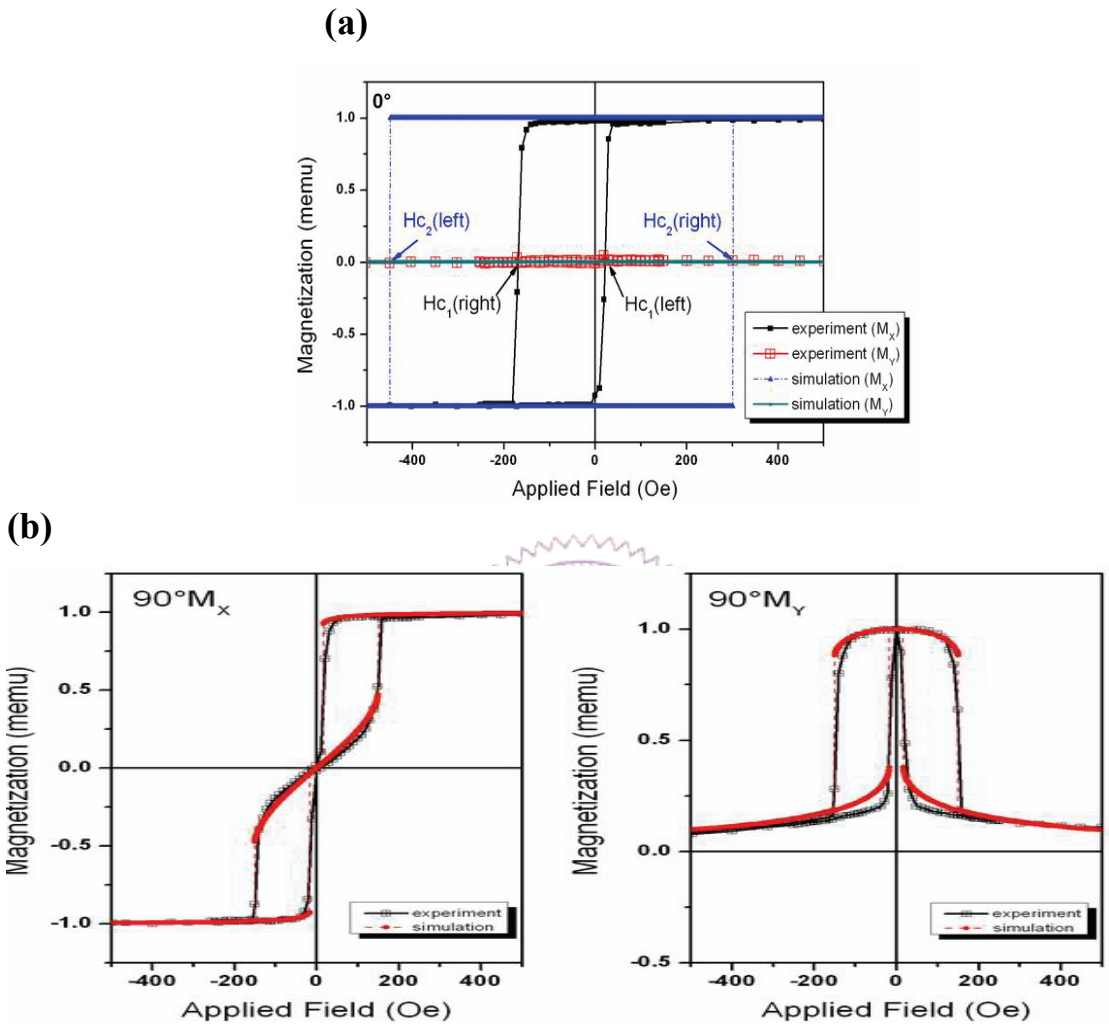

Fig.4.11 the hysteresis loops of (a) θ=0° the hysteresis loops of (a) θ=0° and (b) θ=90°, compared with the simulation curves, the symmetric magnetization reversal in thes two angles occurs by purely domain wall motion and rotation, respectively.

2. Asymmetric Magnetization Reversal

Unlike the equal coercivity difference of both increasing and decreasing field branches, the hysteresis loops measured in other angles between **θ**=0° and 90° seem to show the asymmetric phenomenon from the observing of unequal coercivity difference between increasing and decreasing field branch. When the **θ**=20° and 30°, shown in the Fig. 4.12, the coercivity difference of both M_X loops are larger in the increasing field branches than the decreasing field ones. Furthermore, the M_Y loops also show the same difference in the Figure., which may implies that the magnetization reversal behaves as rotational like in the decreasing fields while it proceeds by domain wall nucleation and growth for increasing fields. However, when the **θ**=60° and 70°, Fig. 4.13, the coercivity difference of M_X and M_Y loops are larger in the decreasing field branches than that in the increasing field ones. Therefore, we suggest that in contrary to the **θ**=20° and 30° cases, the magnetization reversal occurs by moment rotation in the increasing fields while it reverses by domain nucleation and growth for decreasing fields.

In previous reports, the asymmetric magnetization reversal has been observed that the magnetization reversal is different at each branch of the (shifted) hysteresis loop and this asymmetry depends on the angle between the external field and the exchange bias direction. However, less studies have been proposed in the (001) FM/AFM systems, which include the four fold symmetry of magnetocrystalline anisotropy. Recently, in (001) Fe/MnPd system [21], the asymmetric magnetization reversal at **θ**=45° behaves as moment rotational in the decreasing fields while it proceeds by domain wall nucleation and growth for increasing fields. However, this magnetization reversal behavior may not be the same for the angle other

than **θ**=45°. Compared the hysteresis loops of experimental to simulated ones, we suggest that the magnetization reversal described above is valid for $\theta \leqq 45°$; When the $\theta > 45°$, the opposite magnetization reversal occurs by moment rotation in the increasing fields while it reverses by domain nucleation and growth for decreasing fields.

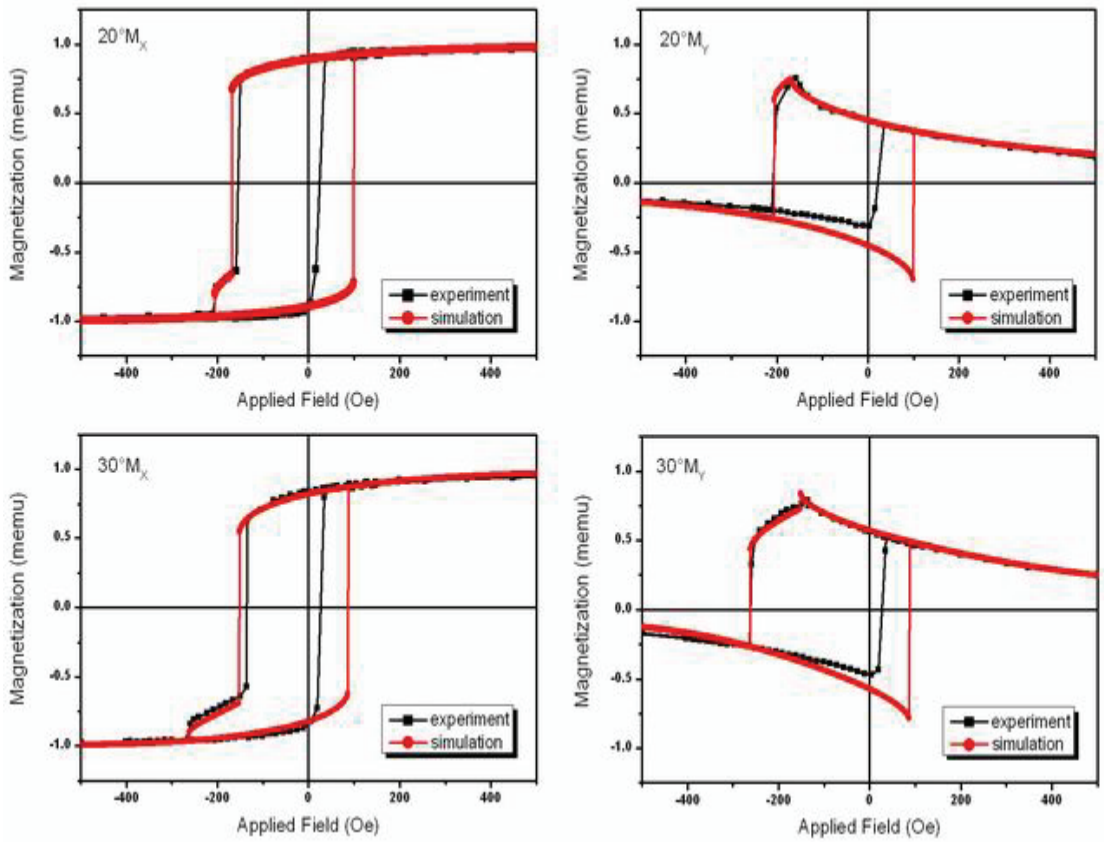

Fig. 4.12 The difference of M_X and M_Y loops between simulated and experimental data measured at **θ**=20° and 30°.

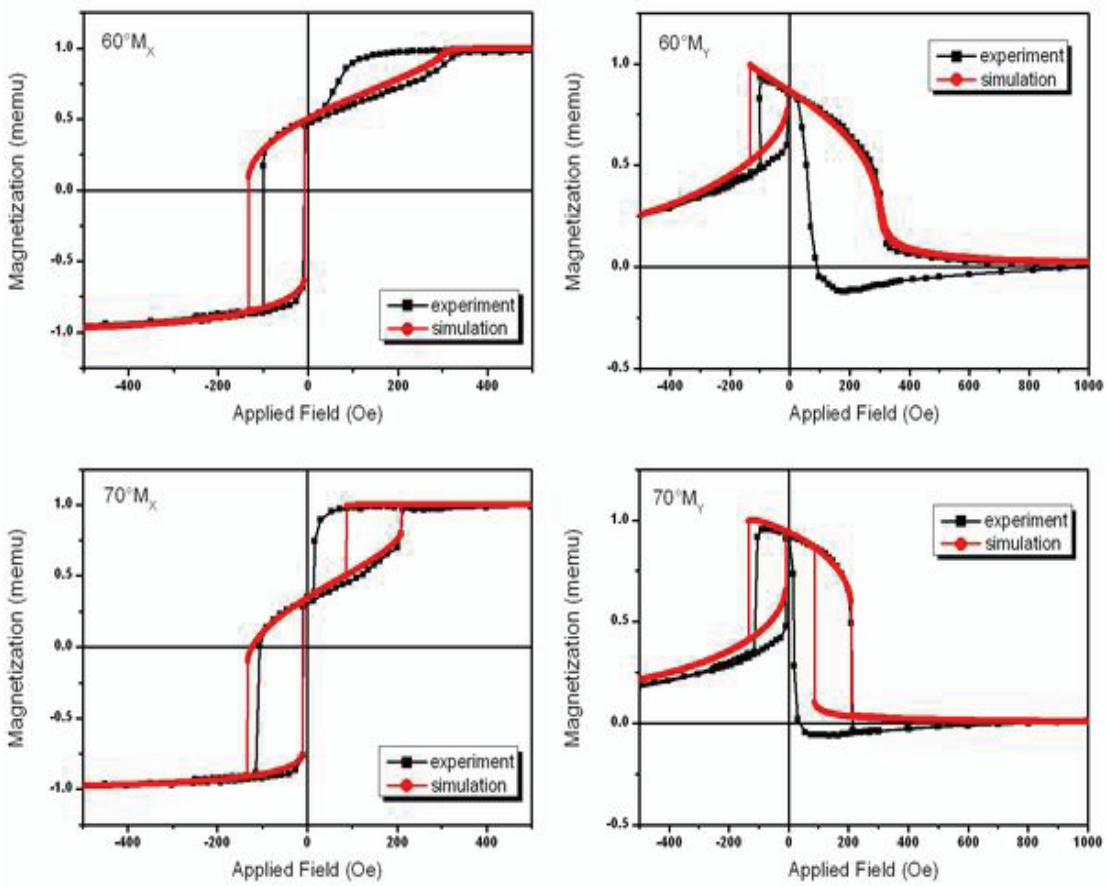

Fig. 4.13 The difference of M_X and M_Y loops between simulated and experimental data measured at θ=60° and 70°.

4.3.d Time dependent effect in (001) IrMn/CoFe system

In (001) IrMn/CoFe system of our experiment, an unusual time-dependent effect was observed when the hysteresis loops were measured with increasing the time scale. The exchange field (H_E) is found to be decreasing and the shape of the hysteresis loop also changes. Although another interesting phenomenon of dreasing the H_E, so called "training effect" (has been introduced in chapter 2) was observed in many FM/AFM systems when they field cycled. However, the training effect seems different from our case, which has drastically changes of the loop shape. Fig. 4.14 shows the magnetic properties of **θ**=0° and **90**° in IrMn(5,10,40nm)/ CoFe(15nm) systems. As compared to the as-deposited film, the sample with smaller IrMn thickness shows a drastical change of the hysteresis loops measured after few days. On the other hand, the much smaller changes were observed for the sample with larger IrMn thickness.

Fig. 4.15 shows the exchange bias field along the CoFe [110] (**θ**=0°), an unusual positive exchange bias fields were observed with increasing the time scale. It seems that we have observed a direction change of unidirectional anisotropy from CoFe [110] to [-110]. In order to verify this phenomenon, the hysteresis loops of other angles between **θ**=0° and **90**° was measured.

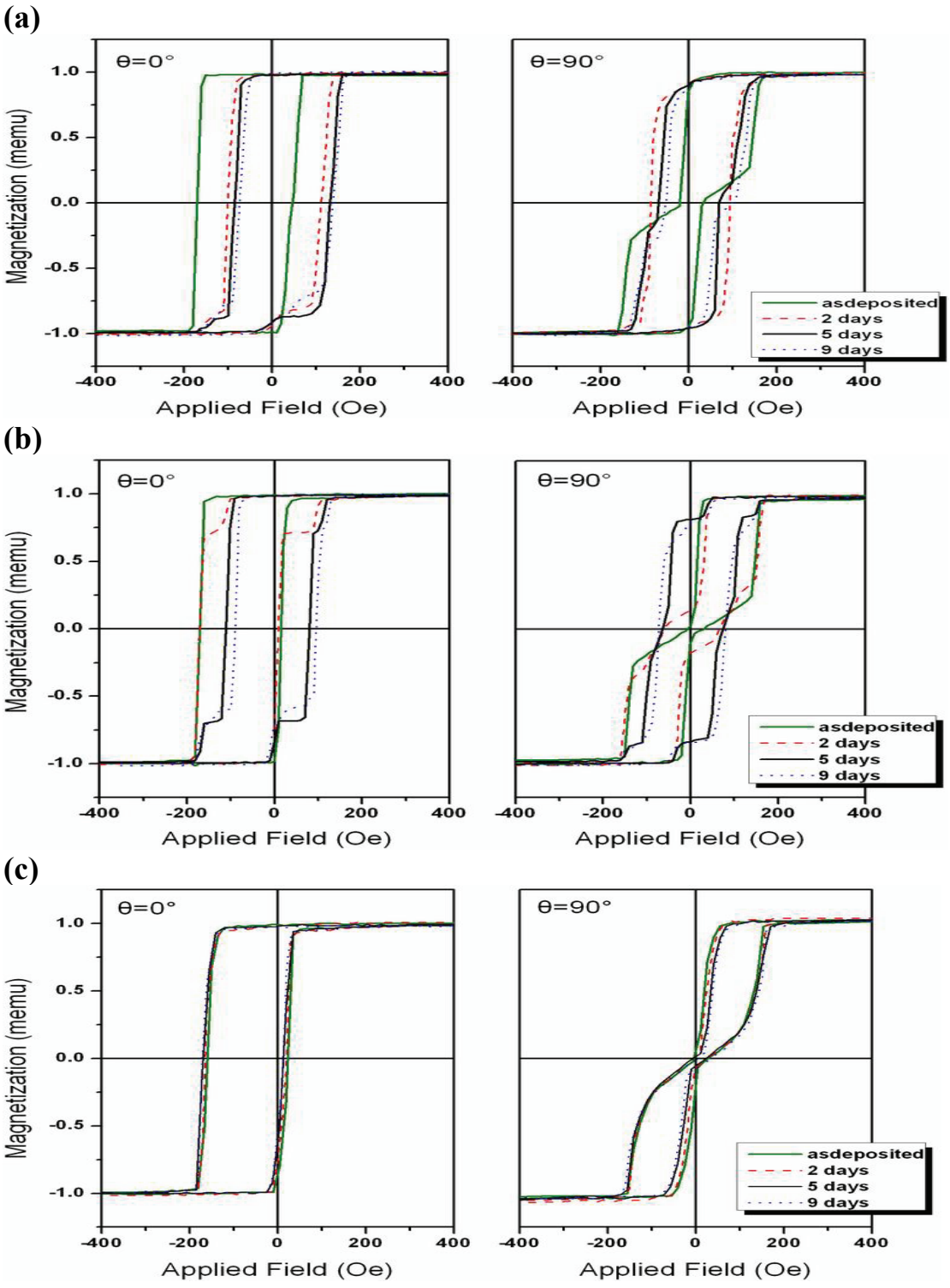

Fig. 4.14 The magnetic properties of **θ**=0° and **90°** in IrMn(5,10,40nm)/ CoFe(15nm) systems. The drastically changes occur in the systems with small thickness of IrMn imply that the change rate depends on the thickness of antiferromagnetic layers.

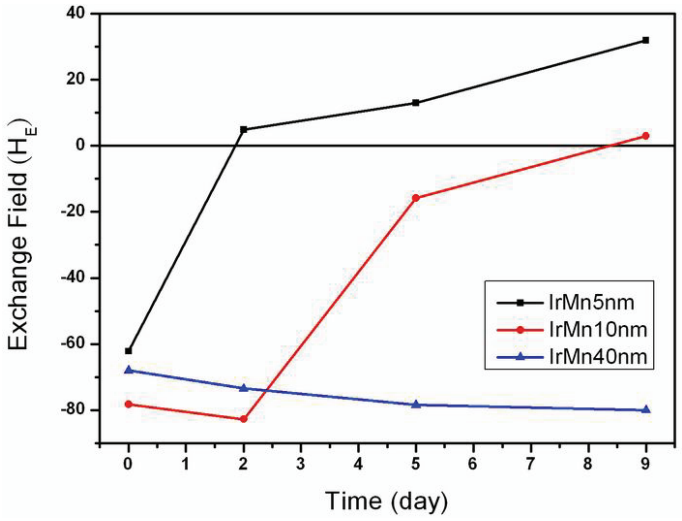

Fig. 4.15 The variation of exchange bias field field (H_E) with increasing the time scale. For the sample with small IrMn thickness, the variation rate are fast and finally show the unusual positive exchange bias fields.

Angular dependence analysis

From the Fig.4.15, the value of exchange bias field (H_E) decreases nearly to the zero after two days from the sample of IrMn (5nm)/ CoFe(15nm) was deposited. Therefore, we investigate the hysteresis loops of both samples of IrMn(5nm)/ CoFe(15nm) that were performed with and without external bias field during the deposition. Fig. 4.16 shows the hysteresis loops measured along the five angles; i.e. θ=0°, 30°, 45°, 60°, 90°. When the time dependent effect occurs, the M_X and M_Y loops of the sample deposited with a bias field are similar to the one deposited without a bias field. So we suggest that the (001) IrMn/CoFe exchange bias system may have a tendency to decreasing the unidirectional anisotropy with increasing time scale so that the magnetization reversal behaves as the samples deposited without the external field. In addition, unlike the as-deposited sample, the negative values of M_Y signal are detected in the increasing field of Fig. 4.16(c) and (e), correlating with the small positive exchange bias field of 5 Oe.

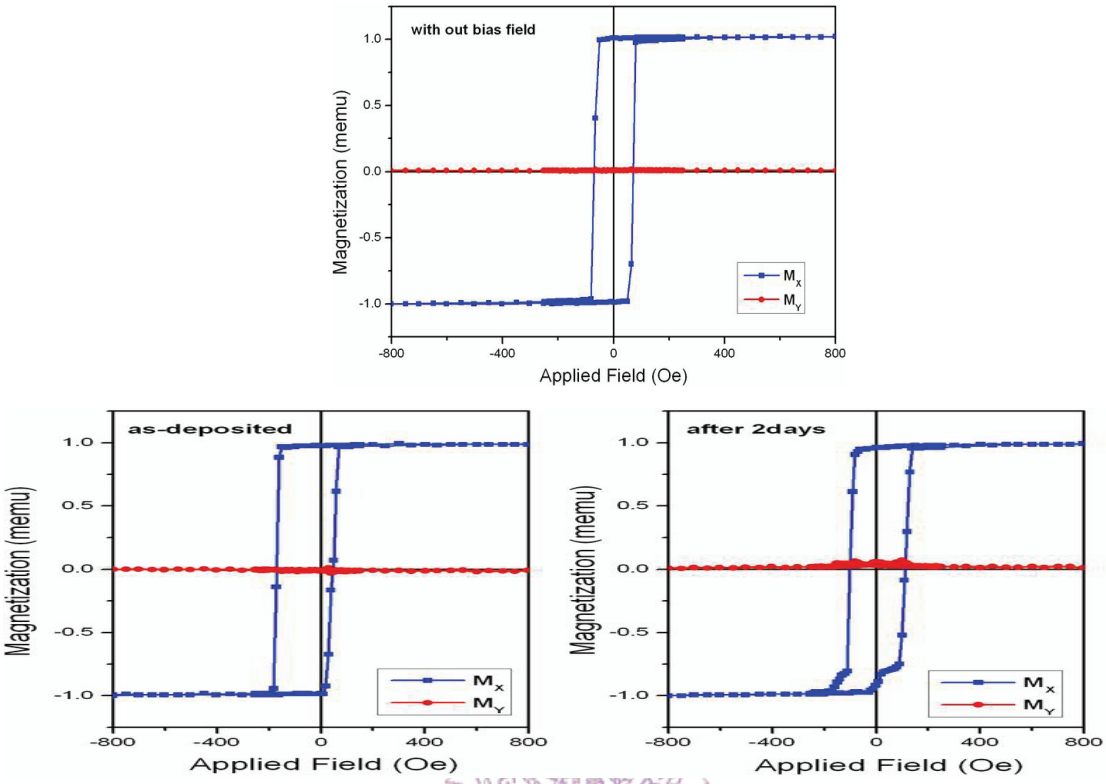

Fig. 4.16(a) The hysteresis loops, which were deposited with and without external bias field of IrMn(5nm)/ CoFe(15nm), were measured at $\theta=0°$.

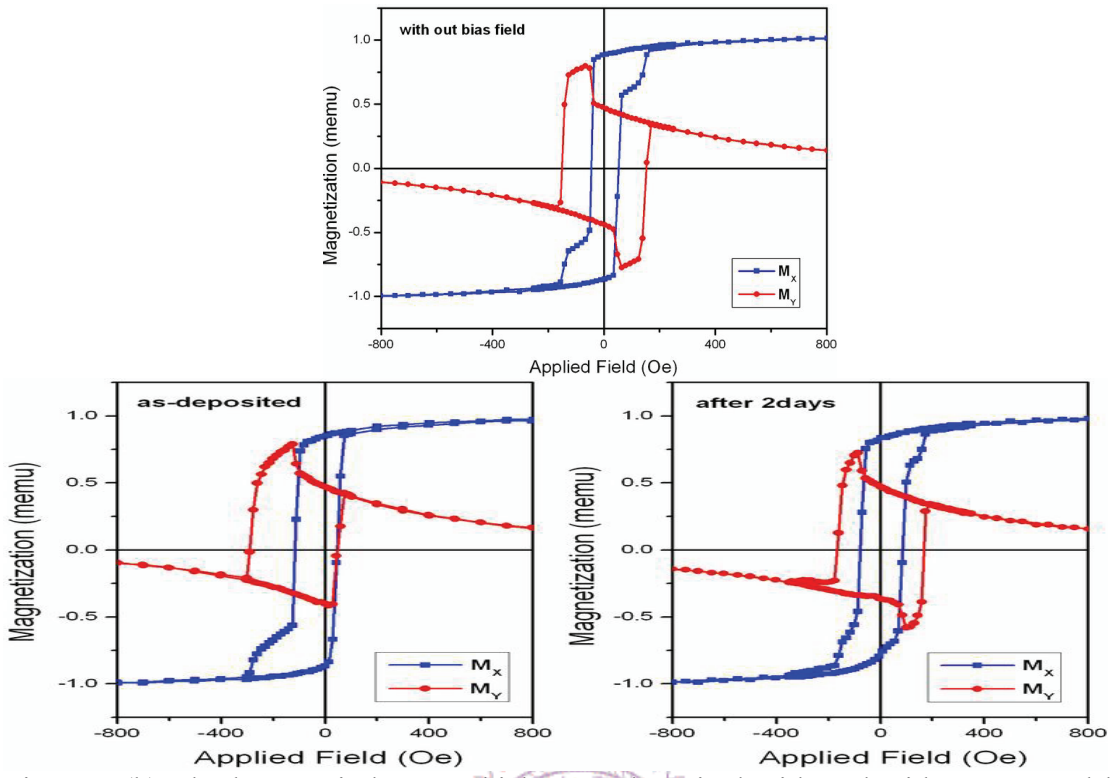

Fig. 4.16(b) The hysteresis loops, which were deposited with and without external bias field of IrMn(5nm)/ CoFe(15nm), were measured at θ=30°.

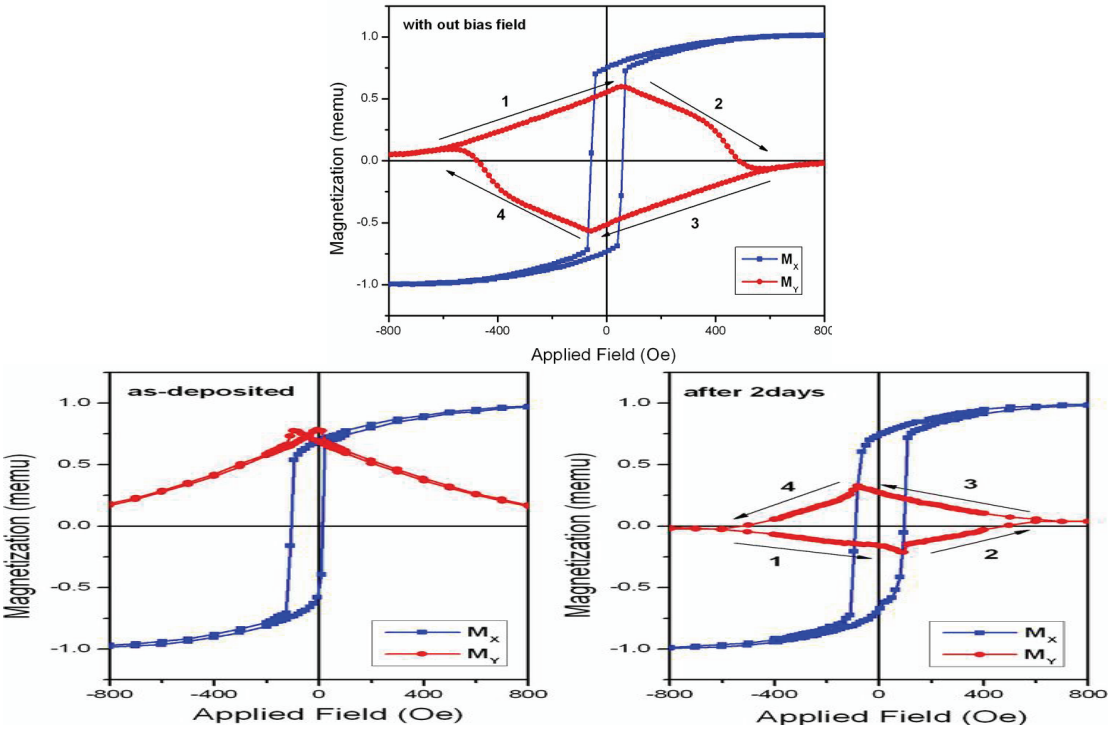

Fig. 4.16(c) The hysteresis loops, which were deposited with and without external bias field of IrMn(5nm)/ CoFe(15nm), were measured at θ=45°.

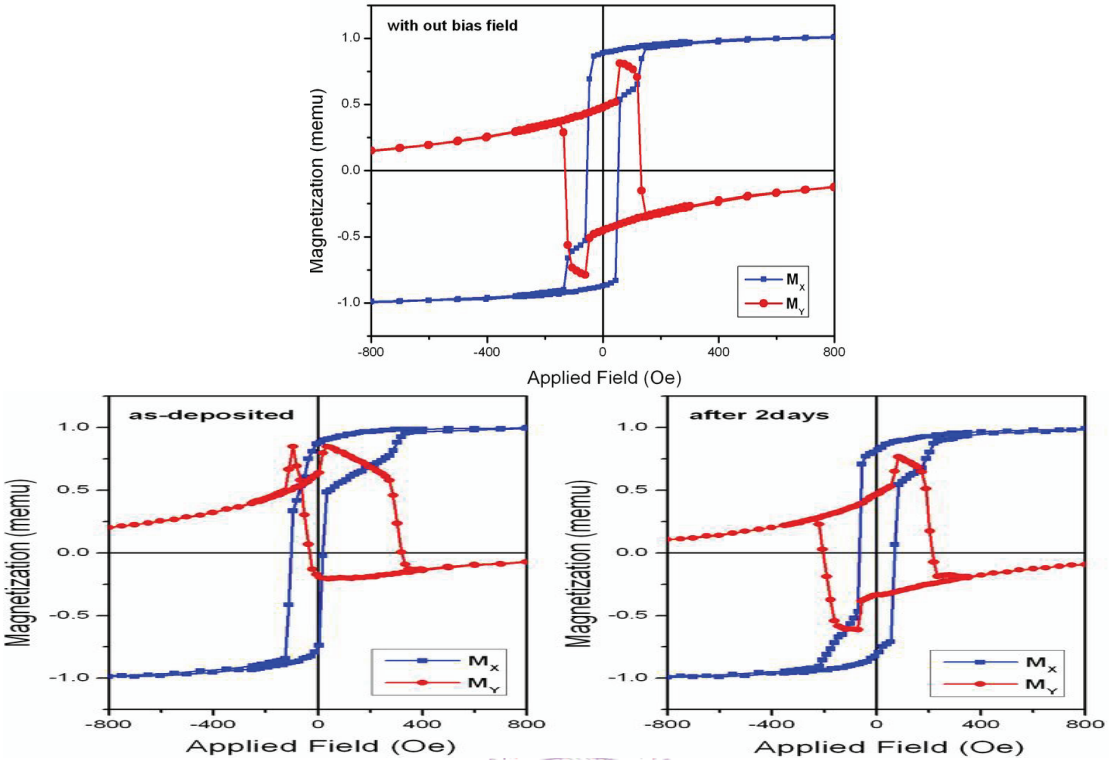

Fig. 4.16(d) The hysteresis loops, which were deposited with and without external bias field of IrMn(5nm)/ CoFe(15nm), were measured at θ=60°.

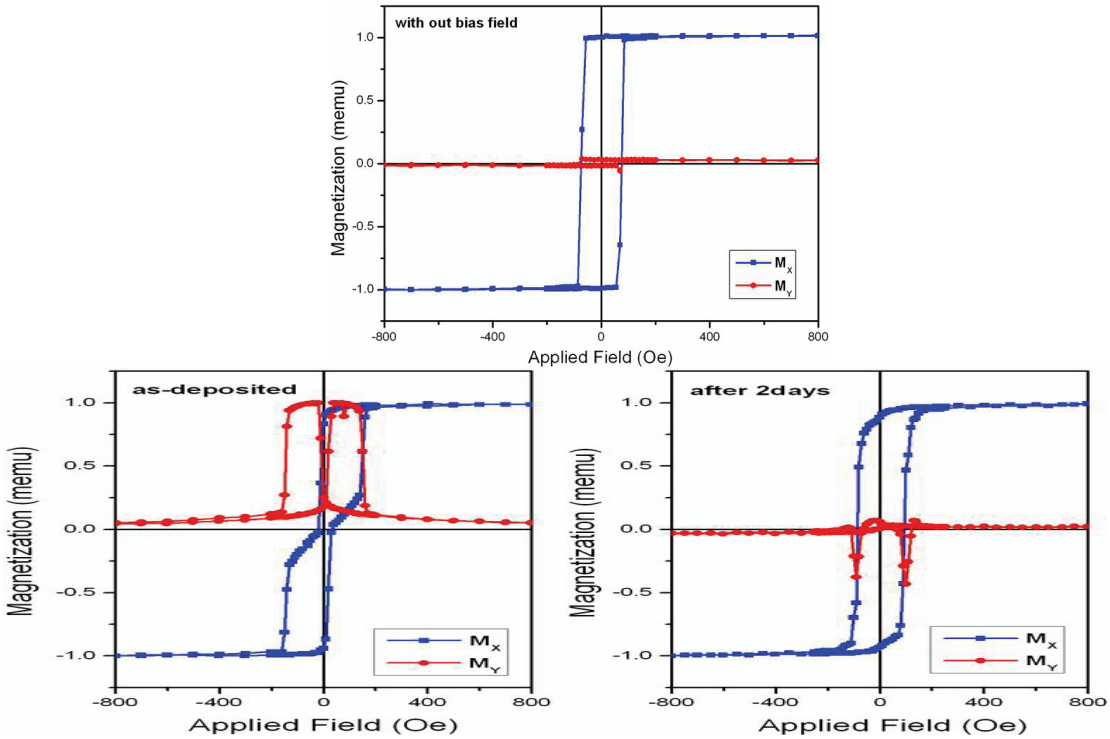

Fig. 4.16(e) The hysteresis loops, which were deposited with and without external bias field of IrMn(5nm)/ CoFe(15nm), were measured at θ=90°.

Possible Reasons for Time dependent effect

1. Stress measurement

To figure out the reason of this phenomenon, we firstly consider to the structure changed by stress relaxation in the epitaxial thin films. Therefore, we performed curvature measurement to analize the relaxation of our sample. As shown in the Fig. 4.17, the in-plane compressive stress was observed since the relationship of the lattice constants in films were $\mathbf{a}_{Cu}<\mathbf{a}_{IrMn}<\sqrt{2}\,\mathbf{a}_{CoFe}$. However, it shows very small curvature changes while the magnetic properties are drastically change. In addition, the X- ray θ-2θ result, as shown in Fig. 4.17, reveal nothing changes with the variation of magnetic properties. Therefore, we suggest that the change of magnetic properties does not have strong relation to the relaxation of epitaxial stress

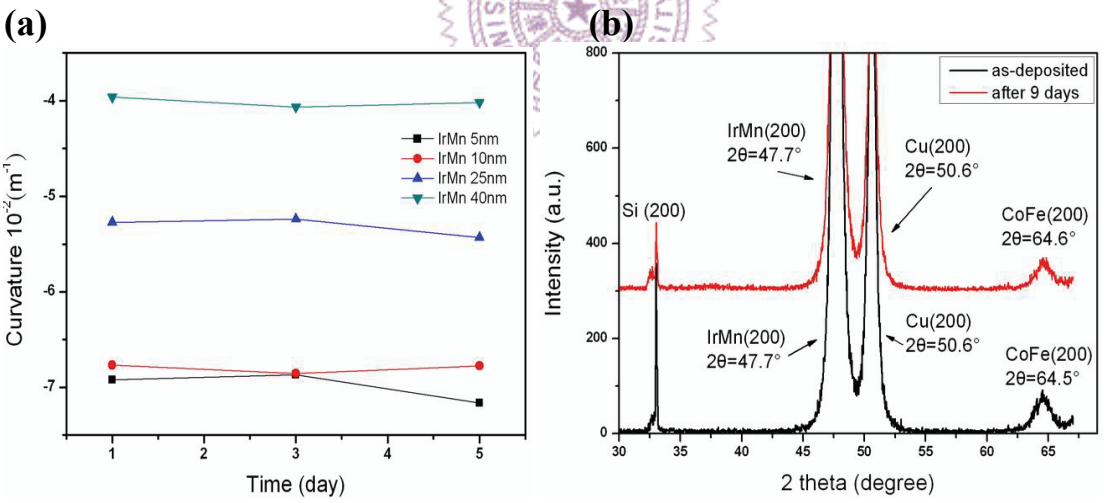

Fig. 4.17 (a) Stress measurements results of IrMn(5,10,25,40nm)/CoFe(15nm). (b) X-ray θ-2θ results of the IrMn(25nm)/CoFe(15nm).

2. Spin Reorientation

In our experiment, the composition of anti-ferromagnetic layer is $Ir_{20}Mn_{80}$, which corresponds to 3Q spin structure as mentioned in chapter2. As shown in Fig. 4.18, the easy axis of IrMn is along IrMn [110], which deviates 45° from the easy axis of ferromagnetic layer (CoFe [110]). However, the spin direction of IrMn at the interface of IrMn/CoFe might be along IrMn [100] by the coupling of ferromagnetic layer in the as-deposited films. It seems that the uncompensated spins of IrMn at the IrMn/CoFe interface may deviate from IrMn [100] since they are in the meta-stable state. When time goes by, the interfacial IrMn spins may switch back to the most stable orientation.

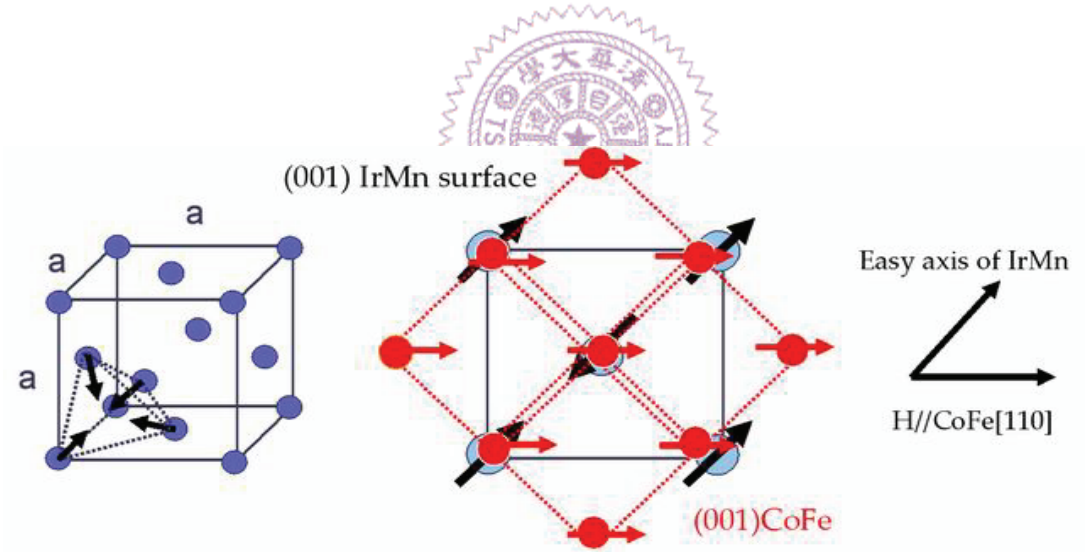

Fig. 4.18 Schematic illustration the relationship of spin orientation between IrMn and CoFe.

4.4 (001) MgO Structures on CoFe

It has been mentioned in chapter 1 that the motivation of our experiment is to obtained the MgO (001) texture by using the (001) IrMn/ CoFe as underlayers. So we finally have demonstrated the (001) MgO structure on the ferromagnetic layer of CoFe. The X-ray θ-2θ results are shown in the Fig. 4.19, the red line represents the sample with Si(001)/ Cu(100nm)/ IrMn(50nm)/ CoFe(30nm)/ MgO(30nm)/ Ta(6nm), indicating a highly texture of (001) MgO from the strong peak of MgO (200) around 2θ=42.5°, corresponding to the lattice constant of 4.256 Å. Therefore, since lattice mismatch between a_{MgO} and $\sqrt{2}\, a_{CoFe}$ is only 4.9%, it is reasonable to understand that the MgO layer may grow epitaxially on CoFe film by rotating 45°. In addition, when we further deposited the CoFe(30nm) on the top of the MgO layer, black line in Fig.4.20, the strong integral intensity of CoFe (200) may imply that we have successfully demonstrated the sample with epitaxial structure of Si/ Cu(001) /IrMn(001) / CoFe(001)/ MgO(001)/ CoFe(001)/ Ta, and Si/ Cu[100] /IrMn[100] / CoFe[110]/ MgO[100]/ CoFe[110] / Ta.

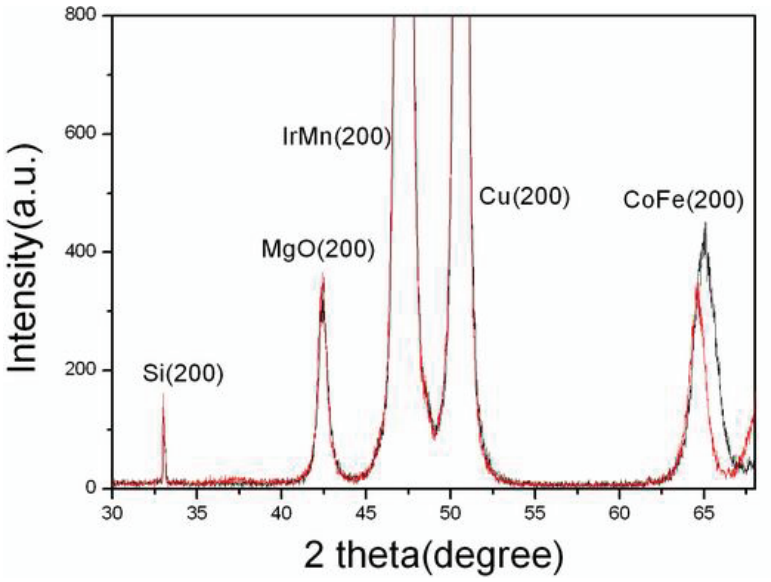

Fig. 4.19 The X-ray θ-2θ results of Si(001)/ Cu(100nm)/ $Ir_{20}Mn_{80}$(50nm)/ CoFe(30nm)/ MgO(30nm)/Ta(6nm), as shown in red line. The stronger integral intensity is shown with the sample of Si(001)/ Cu(100nm)/ $Ir_{20}Mn_{80}$(50nm)/ CoFe(30nm)/ MgO(30nm)/ CoFe(30nm)/ Ta(6nm).